Available online at www.keaipublishing.com/en/journals/journal-of-magnesium-and-alloys/

ScienceDirect

Journal of Magnesium and Alloys 13 (2025) 3632–3641

www.elsevier.com/locate/jma

Full Length Article

Phase transitions, lattice dynamics, thermal transport, and thermodynamic properties of $Mg_2V_2O_7$ from experiments and first-principle calculations[☆]

Guishang Pei[a,b,1], Xin Jin[c,1], Mengjiao Jiao[a,b], Zhuoyang Li[a,b], Dapeng Zhong[a,b], Junyi Xiang[e], Ruixiang Zhu[f], Rui Wang[f], Yuntao Xin[a,b,g,*], Xuewei Lv[a,b,d,*]

[a] *College of Materials Science and Engineering, Chongqing University, Chongqing 400044, China*
[b] *Chongqing Key Laboratory of Vanadium-Titanium Metallurgy and Advanced Materials, Chongqing University, Chongqing 400044, China*
[c] *College of Physics and Electronic Engineering, Chongqing Normal University, Chongqing 401331, China*
[d] *The State Key Laboratory of Mechanical Transmissions, Chongqing University, Chongqing 400044, China*
[e] *College of Metallurgy and Materials Engineering, Chongqing University of Science and Technology, Chongqing 401331, China*
[f] *Institute for Structure and Function & Department of Physics, Chongqing University, Chongqing 400044, China*
[g] *College of Chemistry and Chemical Engineering, Central South University, Changsha 410083, China*

Received 23 July 2023; received in revised form 21 September 2023; accepted 13 November 2023
Available online 23 January 2024

Abstract

$Mg_2V_2O_7$ is the most promising candidate for low-temperature co-fired ceramic (LTCC) multilayer devices. Selecting the appropriate precursors strongly requires reliable thermodynamic properties to be defined accurately. In this study, the structural parameters of the $Mg_2V_2O_7$ at ambient temperature indicate that it is crystallized in space group of $P2_1/c$. Notably, $Mg_2V_2O_7$ has low lattice thermal conductivity (k_L) of 4.77, 5.12, and 4.52 W/mK, along the *a*, *b*, and *c* axes, respectively, which originates from the large phonon scattering rate and low phonon group velocity. The α-$Mg_2V_2O_7\leftrightarrow\beta$-$Mg_2V_2O_7$ and β-$Mg_2V_2O_7\leftrightarrow\gamma$-$Mg_2V_2O_7$ polymorphic transitions occur at 743 °C and 908 °C with enthalpy change of 1.82±0.04 kJ/mol and 1.51±0.04 kJ/mol, respectively. The endothermic effect at 1083 °C with an enthalpy change of 26.54±0.26 kJ/mol is related to the congruent melting of γ-$Mg_2V_2O_7$. In addition, the molar heat capacity of $Mg_2V_2O_7$ was measured utilizing drop calorimetry at high temperatures. The measured thermodynamic properties were then applied to select precursors for preparing $Mg_2V_2O_7$ via a solid-state reaction, indicating that the V_2O_5 and $Mg(OH)_2$ precursors are strongly recommended due to their thermodynamic superiority.

Keywords: $Mg_2V_2O_7$; Phase transitions; Lattice dynamics; Thermal transport properties; Thermodynamic properties.

1. Introduction

The research and development of advanced communications tools, such as mobile phones and laptop computers, strongly require the miniaturization of microwave devices [1–8]. Low-temperature co-fired ceramic (LTCC) multilayer devices can satisfy this requirement. LTCC multilayer devices are composed of alternating dielectric ceramics and internal metallic electrode layers. Ag has generally been utilized for the metallic electrode layer owing to its high conductivity and low cost. However, due to the low melting temperature of Ag at approximately 961 °C, microwave dielectric materials that can be sintered at temperatures below 960 °C should be developed for the fabrication of LTCC devices [9–12]. $Mg_2V_2O_7$ ceramic appears to be a candidate for low-temperature sintering because of its melting temperature (~1100 °C). Joung et al. [13] prepared $Mg_2V_2O_7$ using MgO and V_2O_5 as starting materials through solid-state calcination, and the $Mg_2V_2O_7$ treated at 950 °C for more than 5 h shows low-dielectric constant (ε_r=10.5), high-quality factor

---

[☆] Peer review under the responsibility of Chongqing University.

[*] Corresponding authors.
E-mail addresses: xinyuntao0707@163.com (Y. Xin), lvxuewei@163.com (X. Lv).

[1] These authors contributed equally to this work.

https://doi.org/10.1016/j.jma.2023.11.013

($Q \times f = 58 \times 275$ GHz), and near zero temperature coefficient of resonance frequency (τ_f =-26.9 ppm/ °C), which makes it as an ideal potential candidate for microwave dielectric materials. Although numerous experimental works and theoretical calculations of $Mg_2V_2O_7$ were performed in several times, it is evident that the high-temperature phase of $Mg_2V_2O_7$ is not yet structurally characterized, as well as its lattice dynamics, and thermal transport properties [14].

In addition, the selection of precursors for preparing $Mg_2V_2O_7$ via solid-state calcination significantly impacts the formation mechanism and its microwave dielectric properties. Traditionally, trial and error with various combinations are time-consuming and labor-extensive. Thermodynamic relations control reaction behavior, phase equilibrium, corrosion, *etc*., and it can provide a general guideline for the precursors' selection [15–17]. Therefore, choosing optimum precursors from a thermodynamic viewpoint is necessary before conducting experiments, which need reliable thermodynamic data of all phases to be defined.

Regarding thermodynamic properties of $Mg_2V_2O_7$, Khodos et al. [18] measured molar heat capacity of $Mg_2V_2O_7$ for temperatures ranging from 25 to 300 K using adiabatic calorimetry and derived its entropy at 298 K, which is equal to 212.95 ± 2 $J \cdot mol^{-1} \cdot K^{-1}$. While its molar heat capacity at higher temperatures is still lacking so far. For many stable and metastable compounds, molar heat capacity data are not well experimentally measured at present, especially in the high-temperature range. Traditionally, the CALPHAD community is used to estimate unknown thermodynamic properties by applying the Neumann-Kopp rule [19–22]. This approach assumes a linear combination of simple oxides to predict the desired one. For disordered solid solutions and molten phases, the Neumann-Kopp rule has been proven to be a good approximation in many cases. However, this approach has severe limitations for stoichiometric compounds due to the difference in the electronic structure between the compound and its constituent elements or oxides. To overcome the lack of thermodynamic properties of $Mg_2V_2O_7$ in the literature and known thermodynamic databases, it is nowadays possible to measure the thermodynamic properties based on calorimetric technology, and provide theoretical guidance to materials synthesis.

This study aims to investigate phase transitions, lattice dynamics, thermal transport, and thermodynamic properties of MgV_2O_7 from experiments coupled with first-principle calculations based on density functional theory (DFT), and finally apply the measured thermodynamic data to select the appropriate precursors for preparing $Mg_2V_2O_7$ via solid-state calcination.

2. First-principle calculation methodology

The first-principle calculations were implemented in the Vienna Ab initio Simulation Package (VASP) code [23,24]. The projector augmented wave (PAW) pseudopotential was used as the basis for representing the wave function, and the exchange-correlation function was applied to treat the generalized gradient approximation (GGA) with the Perdew-Burke-Ernzerhof (PBE) function [25,26]. The Monkhorst-Pack [27] scheme with a 5 × 4 × 3 *k*-point grid was used. In the structure relaxation, optimization is performed with an accurate force (a convergence criterion to ensure that the atoms are sufficiently stable in their positions) below 10^{-3} eV/Å and the convergent energy was set to less than 10^{-8} eV. The kinetic energy cutoff was defined as 520 eV. The 2nd-order force constant (FC) was calculated in the finite-displacement method with a 2 × 2 × 1 supercell through PHONOPY [28]. Furthermore, the 3rd-order FC was obtained employing the third-order scripts, and the thermal conductivity was also calculated with the ShengBTE package [29]. For achieving the convergence of thermal conductivity, the q-grid mesh is set to 6 × 5 × 4 for $Mg_2V_2O_7$ [30].

3. Materials and experimental methods

3.1. Sample preparation

In this study, magnesium oxide (MgO) and vanadium pentoxide (V_2O_5) with a purity of 99.99% and 99.95%, respectively, were used as the starting materials. Prior to weighting, the MgO and V_2O_5 powders were calcinated at 1173 K and 573 K, respectively, for 5 h to eliminate any absorbed moisture and other impurities. Subsequently, The $Mg_2V_2O_7$ powder was synthesized by roasting and milling process with the fixed molar ratio MgO and V_2O_5 of 2:1. The homogenous mixtures were compacted into disks with a hydraulic press of 80 MPa and then were heated to 650 °C with heating rate of 10 °C /min in muffle and maintained for 48 h in air. After that, the pellets were cooled down to room temperature in the switched-off furnace. The calcinated samples were pulverized in a vibration mill and roasted after pressing to a disk form again at 700 °C, and 750 °C. The facile solid-state calcination completely proceeds by repeating intermediate grinding and roasting at 750 °C twice, which guarantees that no other phases exist, and high-pure desired samples are finally prepared.

3.2. Sample characterizations

3.2.1. X-ray diffraction (XRD)

Powder X-ray diffraction (XRD, PANalytical X'Pert Powder, PANalytical B.V.) using Cu Kα radiation (λ=0.154 nm, 40 kV, 75 mA) was conducted to identify the phase composition of the prepared $Mg_2V_2O_7$ at ambient temperature. The XRD measurements were operated over diffraction angle range of 10°-70° with a relatively slow scanning step of 0.14°/min. The phase composition of $Mg_2V_2O_7$ at higher temperatures was also checked by performing *in-situ* XRD measurements. The powder sample needs to be dissolved in alcohol and then dropped in a Pt flake to carry out experiments at higher temperatures with a specific temperature interval of 100 °C. The diffraction patterns measured at higher temperatures were further analyzed by employing the HighScore

Plus software package coupled with the Rietveld refinement method.

3.2.2. Fourier transform infrared (FTIR)

Fourier transform infrared (FTIR) spectrophotometer (Spectrum 100, PerkinElmer) was applied for measuring the FTIR transmission spectrum of the as-prepared $Mg_2V_2O_7$ sample. The impedance analyzer was utilized for the determination of frequency-dependent ac conductance, impedance, dielectric constant, capacitance, inductance, and reactance.

3.2.3. Scanning electron microscopy (SEM)

Scanning electron microscopy (SEM, TESCANVEGA 3 LMH, Czech Republic), was used for observation of surface morphology and particle size of the as-prepared $Mg_2V_2O_7$ sample.

3.2.4. Inductively coupled plasma optical emission spectroscopy (ICP-OES)

An inductively coupled plasma optical emission spectroscopy (ICP-OES) analysis, using an Optima 8000 Instrument (PerkinElmer, USA), was carried out to quantitatively determine the vanadium content of the as-prepared sample.

3.3. Phase transitions and thermodynamic properties measurements

In this study, temperatures and its enthalpy changes of the polymorphic transitions and melting of the $Mg_2V_2O_7$ were determined by DSC methods. The measurements were conducted on a NETZSCH DSC 404 F3 Pegasus thermal analyzer for temperature ranging from ambient temperature up to 1200 °C with heating rates of 5, 10, 15 °C /min and flow rate of 50 mL/min under argon atmosphere. The maximum uncertainties on DSC instrument of temperature measurements lie within ±2 °C and enthalpy change ±2.0%, which was established by determining standard material Aluminum (99.999%, 12 mg±1 mg), Zinc (99.999%, 12 mg ±1 mg), Tin (99.999%, 12 mg±1 mg), and Indium (99.999%, 12 mg±1 mg). The error is calculated by comparing the measured average values and standard values [31–33].

The high-temperature enthalpy increments of the $Mg_2V_2O_7$ were experimentally measured using an isothermal MHTC 96 line calorimeter (SETARAM, France). Calorimetric experiments were performed with a drop sensor using sapphire (α-Al_2O_3) as reference material under flowing helium with purity above 99.999% [34]. The $Mg_2V_2O_7$ samples were pre-treated to 4 small samples for measurements which were cubic shapes with pieces of typical mass between 80 and 100 mg. Samples were dropped into an alumina crucible at the preset temperature, which does not react with the $Mg_2V_2O_7$ below 1450 K, The details of the calorimetric measurements and basic principle were described elsewhere [35–37].

The applicability and reliability of the MHTC 96 line were verified by molar heat capacity measurements of Nickel (99.999%) for the temperature ranging of 373-873 K, and α-Al_2O_3 was also used as reference standard material. Deviations of the experimental results from the standard values lie at ±2.0%, as compared with the values given by the former National Bureau of Standards [38]. The characteristics of $Mg_2V_2O_7$ were measured at selected temperatures 500 K and 1000 K so that the reliability and repeatability of the calorimetric process were then confirmed. The measurement error did not exceed 0.5% and 0.8% at 500 K and 1000 K, respectively.

4. Results and discussion

4.1. Phase structure, lattice dynamics, and materials characterization

XRD patterns was recorded to verify the phase component and crystal structure of the prepared $Mg_2V_2O_7$ sample. The XRD results and conventional crystal structure are presented in Fig. 1(a) and 1 (b), respectively. As seen in Fig. 1(a), the peaks recorded for the $Mg_2V_2O_7$ can be well indexed in comparison with a standard PDF card (*No* 96-900-9747). No foreign diffraction peaks of other phases were found in the

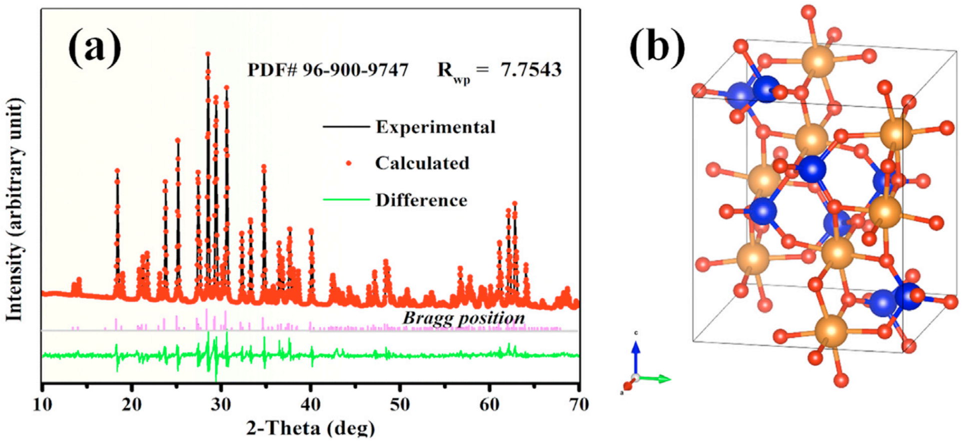

Fig. 1. XRD patterns (a) and conventional crystal structure (b) of monoclinic $Mg_2V_2O_7$.

Table 1
The calculated unit cell parameters *a, b, c, β*, and cell volume of $Mg_2V_2O_7$ along with experimental data.

Method	*a* (Å)	*b* (Å)	*c* (Å)	*β* (°)	Volume (Å^3)
Expt.	6.605(4)	8.415(6)	9.487(2)	100.62(7)	518.3
PBE	6.718	8.531	9.617	100.858	541.307
PBE (error)	1.6%	1.3%	1.4%	0.2%	4.3%

2θ range of 10-70°. Quantitative analysis with the Rietveld refinement method was done by comparing XRD standard patterns and the measured one in this work, and the R_{wp} is 7.4470%, the low values obtained for both R_{wp} (7.75%) indicate a high refinement quality. The mass percent of the prepared $Mg_2V_2O_7$ sample was approximately 99.5%. $Mg_2V_2O_7$ crystallizes in monoclinic system space group $P2_1/c$, with the cell parameters of $a = 6.605(4)$ Å, $b = 8.415(6)$ Å, $c = 9.487(2)$ Å, and β=100.62(7)°, respectively. The quantitative analysis was also performed by ICP-OES, which indicates that the molar percent content of MgO and V_2O_5 is 66.66% and 33.34%, respectively.

Fig. 1(b) is the conventional crystal structure of the monoclinic $Mg_2V_2O_7$ containing MgO_6 octahedra and VO_4 tetrahedra. The optimized cell parameters *a, b, c*, and *β* are tabulated in Table 1, and the values match closely with the experimentally measured ones, confirming the reliability of the theoretical calculations in this work. Besides, phonon dispersion curves are calculated to drive the lattice dynamic and thermophysical properties of the $Mg_2V_2O_7$. The structure contains 44 atoms per primitive cell, therefore, there are 132 phonon branches (three acoustic and 129 optical branches) in the phonon dispersion curve as illustrated in Fig. 2(a). No imaginary frequency phonon modes are observed, which manifests the dynamic stability of $Mg_2V_2O_7$. Additionally, the acoustic and optical phonon modes severely overlap in the low-frequency range, as seen in Fig. 2(a). This can lead to large three-phonon scattering channels for heat-carrying acoustic phonons, shown in Fig. 2(b) as well.

Nanoscale structures are typically formed when sintering at a relatively low temperature (<1000 °C) via solid-state fabrication [39], which are not suitable for calorimetric measurements due to some uncertain impact contributed by surface energy [40,41]. The grain size of the prepared sample should be evaluated before conducting calorimetric experiments. The XRD instrument background was deduced and a standard sample with a grain size of 5~20 μm was initially tested to correct the instrumental peak broadening term. The average grain size (D) and microstrain (ε) of $Mg_2V_2O_7$ were estimated with the use of the Scherrer's formula:

$$D = K\lambda/\beta cos\theta \tag{3}$$

where λ is the wavelength of Cu Kα radiation, K is the shape factor (K = 0.94), β is the full width at half maximum of the selected peak, and θ is the angle position of the selected peak. The calculated crystallite size of $Mg_2V_2O_7$ (~64 nm) is larger than that of the typical value of nanoscale materials (20 nm). Therefore, it can be used for the follow-up calorimetric determination.

FTIR spectroscopy is an analytical technique that provides significant information about the chemical bonding and phase formation of materials, whether organic or inorganic [42–45]. It also provides information about the vibration frequency of efficient groups, network configurations of samples, and cation situations in oxides. Fig. 3 shows the FTIR spectra of the synthesized $Mg_2V_2O_7$. It was reported that the V = O stretch in crystalline V_2O_5 gives rise to a sharp and intense band at 1020 cm^{-1} [31], while no obvious peaks around 1020 cm^{-1} can be identified in the observed spectra. Several weak bands around 2000 cm^{-1} are found which might be contributed by the existing MgO. Another band observed at 1630 cm^{-1} can be assigned to the absorbed water. As shown in Fig. 3, six bands centered at 964, 917, 806, 655, 517, and 437 cm^{-1} are observed in the synthesized $Mg_2V_2O_7$. The FTIR spectrum of the synthesized samples corresponds to those reported previously for $Mg_2V_2O_7$ [32,33].

Surface morphology and particle size of the $Mg_2V_2O_7$ sample were characterized by utilizing SEM. Some charac-

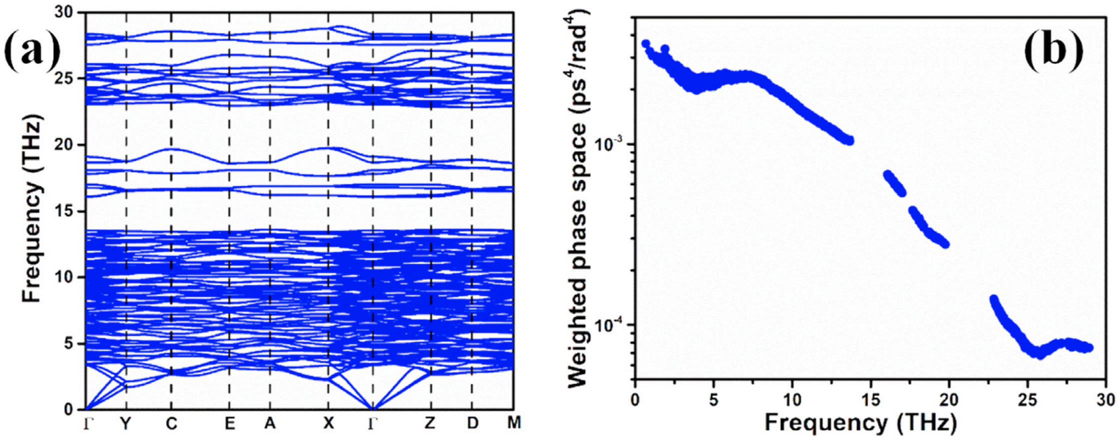

Fig. 2. Phonon dispersion curves along high-symmetry directions of the Brillouin zone (a) and Frequency-dependent weighted three-phonon scattering phase space (b) of $Mg_2V_2O_7$.

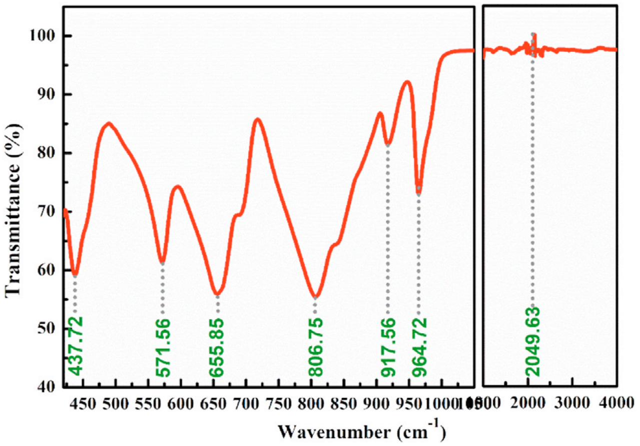

Fig. 3. FTIR spectrum of $Mg_2V_2O_7$ sample.

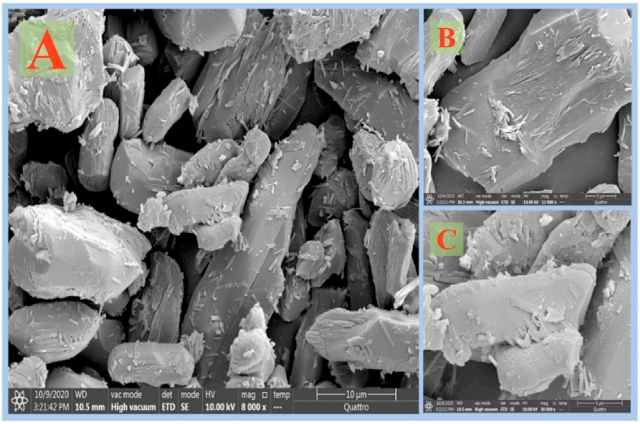

Fig. 4. SEM images of the as-prepared $Mg_2V_2O_7$ particles.

teristic micrographs were observed at three different magnifications, and the SEM patterns are given in Fig. 4. These micrographs reveal agglomerates of particles shaped in small chunks. The grain size can be estimated in the image of × 8000 magnification. The major particle morphology is a regular polygon, with a corresponding average size of 50 μm.

4.2. Thermal transport properties

The thermal transport properties of $Mg_2V_2O_7$ are the key factor to determine its heat dissipation and safety in various applications such as microwave dielectric. Hence, it is crucial to quantitatively comprehend the intrinsic thermal transport characteristics of $Mg_2V_2O_7$ and its underlying physical mechanisms. The previous study [46] experimentally confirms that $Mg_2V_2O_7$ is a semiconductor with an indirect bandgap of approximately 3.0 eV, indicating that lattice thermal conductivity can be considered as the total thermal conductivity. Based on the second-order and third-order FC, phonon transport properties of the $Mg_2V_2O_7$, including the phonon scattering rate (τ^{-1}) and lattice thermal conductivity (k_L) by performing first-principles calculations and PBTE theory, were systematically studied in this work. Fig. 5(a) displays the k_L of $Mg_2V_2O_7$ along different axes, as calculated within the PBTE framework. Notably, at ambient temperature, $Mg_2V_2O_7$ has low k_L values of 4.77, 5.12, and 4.52 W/mK along the *a, b*, and *c* axes, respectively, and it originates from the large τ^{-1} and low phonon group velocity (v_g), as seen in Fig. 5(b) and (c). Such low k_L might be due to the strong anharmonicity of $Mg_2V_2O_7$ aroused from the bonding inhomogeneity contributed by strong V-O bonds and weak Mg-O bonds. The thermal transport properties of $Mg_2V_2O_7$ through first-principles calculations are crucial for better understanding of its further applications in the field of semiconductors.

4.3. Phase transitions

The heat flow curves of the $Mg_2V_2O_7$ sample across the phase transition region with the specific heating rate of 5, 10, and 15 °C /min under an Air atmosphere are presented in Fig. 6. There are three obvious endothermic peaks corresponding to two polymorphic transitions and one congruent melting. The endothermic peak area becomes larger with increasing heating rates, while, the transition temperatures are not changed at all. The polymorphic transitions of α-$Mg_2V_2O_7 \leftrightarrow \beta$-$Mg_2V_2O_7$ and β-$Mg_2V_2O_7 \leftrightarrow \gamma$-$Mg_2V_2O_7$ occur at 743 °C and 908 °C on average, respectively. The temperature of polymorphic transition

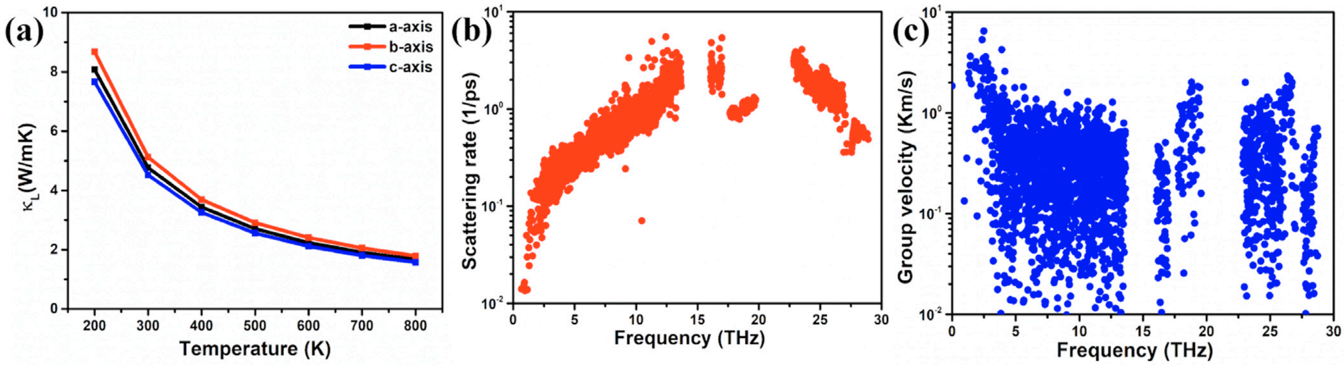

Fig. 5. The temperature-dependent k_L along *a, b*, and *c* axes, predicted from the PBTE theory (a), the scattering rate (τ^{-1}) calculated at room temperature (b), and the frequency-dependent group velocity along *a* axis (c) of $Mg_2V_2O_7$.

Table 2
Phase transitions and related temperature in $Mg_2V_2O_7$.

Phase transitions		Temperature (°C)	References
Polymorphic transitions	α-$Mg_2V_2O_7$↔β-$Mg_2V_2O_7$	738	Wollast et al. [47]
		720	Clark et al. [48]
		720	Cao et al. [49]
		743	This work
	β-$Mg_2V_2O_7$↔γ-$Mg_2V_2O_7$	917	Wollast et al. [47]
		910	Clark et al. [48]
		912	Speranskaya et al. [51]
		911	Pollard et al. [50]
		913	Cao et al. [49]
		908	This work
Congruent melting		1093	Wollast et al. [47]
		1083	This work

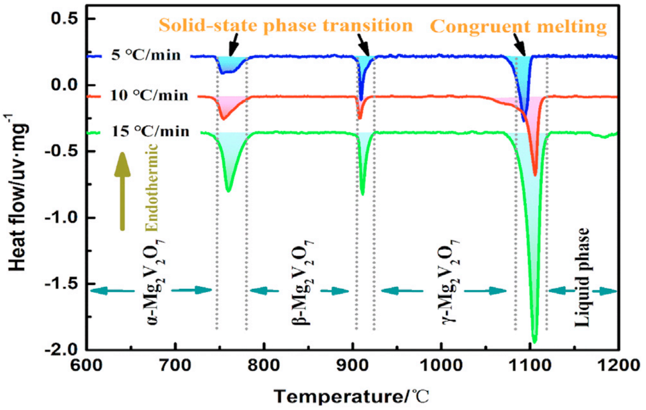

Fig. 6. Heat flow curves of the as-prepared $Mg_2V_2O_7$ sample with various heating rates.

α-$Mg_2V_2O_7$↔β-$Mg_2V_2O_7$ was also reported by Wollast et al. [47] (738 °C), Clark et al. [48] (720 °C), and Cao et al. [49] (720 °C). It can be seen that the value measured in this study is about 23 °C higher than that of Clark et al. [48]. Unfortunately, the purity and XRD patterns of the prepared $Mg_2V_2O_7$ sample were not mentioned in their work, and therefore, it may be questionable more or less. The present result regarding α-$Mg_2V_2O_7$↔β-$Mg_2V_2O_7$ transition is well consistent with that of Wollast et al. [47] (738 °C). The β-$Mg_2V_2O_7$↔γ-$Mg_2V_2O_7$ structural transition was also previously reported by Wollast et al. [47] at 917 °C, Pollard et al. [50] at 910 °C, Speranskaya et al. [51] at 912 °C, Clark et al. [48] at 911 °C as well as Cao et al. [49] at 913 °C. The transition temperature measured in the present study is consistent with the previously reported one. The polymorphic transition temperature by Cao et al. [49] (α-$Mg_2V_2O_7$↔β-$Mg_2V_2O_7$ at 720 °C and β-$Mg_2V_2O_7$↔γ-$Mg_2V_2O_7$ at 913 °C) were obtained by thermodynamically assessing the MgO-V_2O_5 system based on critical evaluation of all available phase diagram data and thermodynamic properties simultaneously, which are optimized data instead of experimental results. The present result is more reliable and can be utilized in the future with confidence. In terms of congruent melting, the experimental results verify that congruent melting of γ-$Mg_2V_2O_7$ occurs around 1083 °C, which is in agreement with the results of Wollast et al. [47] (1093 °C). All available results from the literature and present study are tabulated in Table 2. The enthalpy changes of the polymorphic transitions and congruent melting were also determined by integrating endothermal peaks, the average values are equal to 1.82±0.04 kJ/mol, 1.51±0.04 kJ/mol, and 26.54±0.26 kJ/mol corresponding to α-$Mg_2V_2O_7$↔β-$Mg_2V_2O_7$, β-$Mg_2V_2O_7$↔γ-$Mg_2V_2O_7$, and congruent melting, respectively.

In-situ XRD patterns of the $Mg_2V_2O_7$ sample at temperatures between 25-1000 °C, as recorded in the 2θ range of 15-45°, are presented in Fig. 7(a). Fig. 7(b) is the enlarged view of the diffraction peak in the 2θ range of 27-30°. The XRD patterns of the prepared α-$Mg_2V_2O_7$ are well indexed in comparison to the standard card (No 31-0816), and they are not significantly changed below 700 °C. However, some slight deviations in diffraction peak position and intensity can still be detected in the enlarged view as shown in Fig. 7(b). The position of the predominant peak in the 2θ range of 27-30° is slightly shifted to lower angles, affirming that the cell parameters of the sample increase at higher temperatures. It may be caused by lattice expansion due to temperature increase. The diffraction patterns at 800 °C is dramatically different compared to those at lower temperatures, and it indicates the transformation into a new polymorphic modification β-$Mg_2V_2O_7$. The observed XRD patterns of β-$Mg_2V_2O_7$ match well with the standard PDF card (No: 40-0164). The refinement of cell parameters indicated that the β-$Mg_2V_2O_7$ is crystallized in a triclinic space group $P1$ with the cell parameters of $a = 13.759(3)$ Å, $b = 5.435(5)$ Å, $c = 4.930(2)$ Å, α=81.431(6)°, β=106.892(8)° and γ=130.359(5)°. Next polymorphic phase γ-$Mg_2V_2O_7$ is formed when temperature is over 1000 °C. In-situ XRD patterns of $Mg_2V_2O_7$ are consistent with the results of DCS investigation.

4.4. Thermodynamic properties

Enthalpy increments curve at the specific temperature measurement sequence is typically composed of four drops of the studied samples and four drops of the sapphires (α-Al_2O_3) used as ϕ standard material. The heat flow single continu-

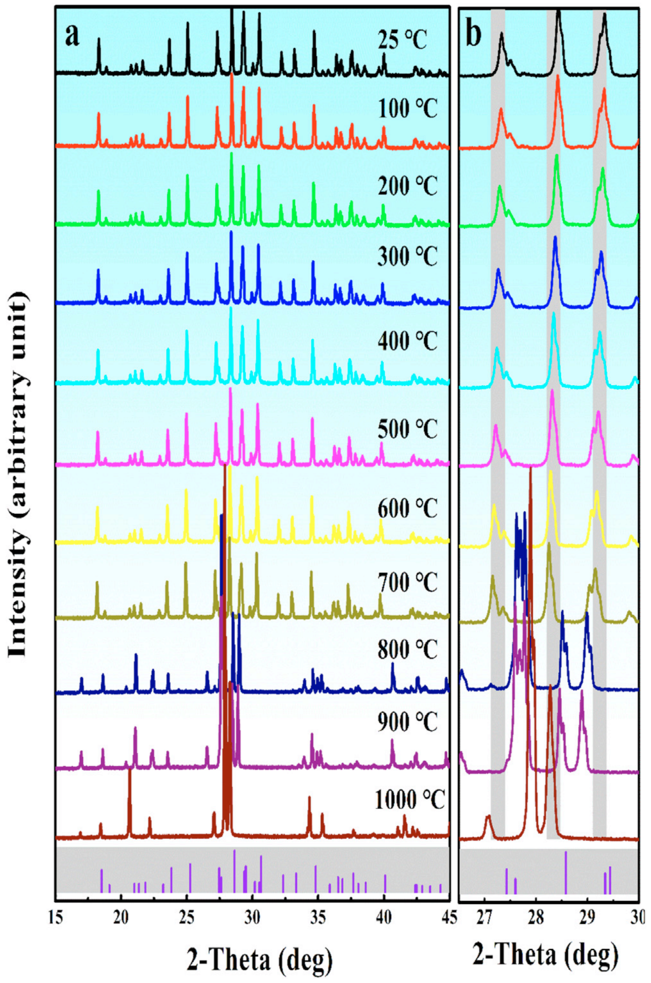

Fig. 7. XRD patterns of $Mg_2V_2O_7$ at high temperatures: (a) Full version in the 2θ range of 15–45°, and (b) the enlarged view of diffraction peak in the 2θ range of 27–30°.

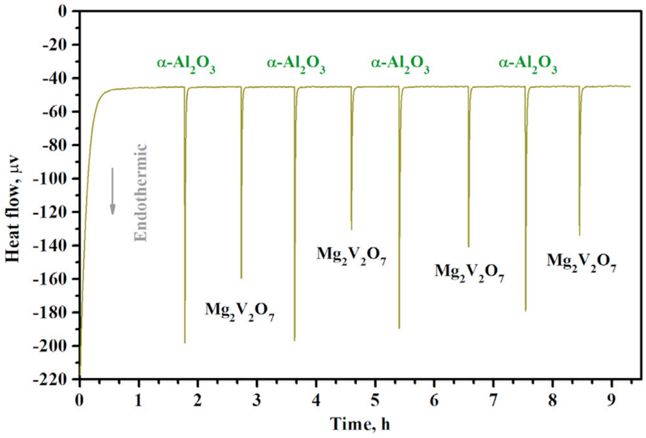

Fig. 8. The heat flow of (α-Al_2O_3) and $Mg_2V_2O_7$ at 773 K.

ously recorded at 773 K at 1 atm is presented in Fig. 8, serial number I, III, V, and VII denote the endothermic peak of the sapphire, while thermal events with numbers II, IV, VI, and VIII are related to the studied sample $Mg_2V_2O_7$. All endothermic peaks of the heat flow curve were individually integrated by employing Calisto data collection & analysis software to compute the enthalpy increment after the dropping process at various experimental runs.

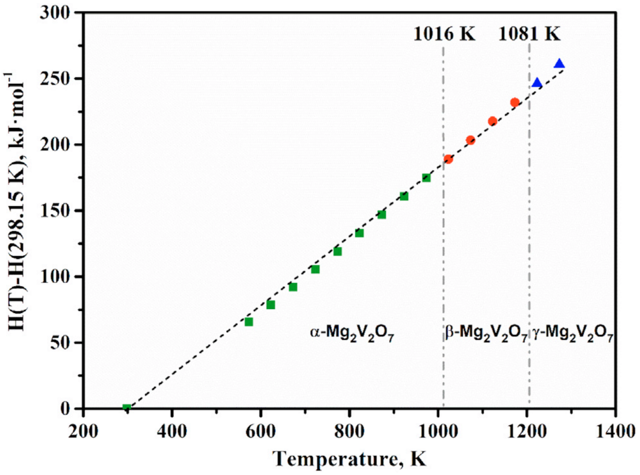

Fig. 9. The original and fitted enthalpy changes of $Mg_2V_2O_7$, as obtained by drop calorimetry.

All experimental results were listed in Table 3 and plotted in Fig. 9 as well. To fit the experimental data as one expression at high temperature, the enthalpy changes of the polymorphic transitions (α-$Mg_2V_2O_7 \leftrightarrow \beta$-$Mg_2V_2O_7$ and β-$Mg_2V_2O_7 \leftrightarrow \gamma$-$Mg_2V_2O_7$,) were subtracted when computing the enthalpy increments of the sample above each transition. All experimentally measured values were fitted by a least squares method based on a modified Maier-Kelley polynomial [52]:

$$\Delta H = aT + b/2T^2 - cT^{-1} + d \qquad (J \cdot mol^{-1}) \tag{1}$$

where a, b, c, and d are the parameters.

The molar heat capacity is equal to the enthalpy variation divided by the temperature variation for temperatures ranging from 298.15 to 1273 K. Then, the corresponding standard expression for Cp,m can be obtained as follows:

$$Cp, m = 259.19657 + 0.03105T - 5781130T^2 \qquad (J \cdot mol^{-1} \cdot K^{-1}) \tag{2}$$

The fitted molar heat capacity curve is presented in Fig. 10. The molar heat capacity is calculated taking into account all measured enthalpy data using a simultaneous linear regression present in Table 1 along with the low-temperature heat capacity determined by Khodos et al. [18] at 298.15 K. The maximum error is within 2% and the mean error lies at 1%. As above mentioned, the low-temperature molar heat capacity of $Mg_2V_2O_7$ between 25-300 K was experimentally determined using adiabatic calorimetry by Khodos et al. [18], and based on the obtained low-temperature molar heat capacity, they also calculated the entropy at 298 K. Temperature dependence of the high-temperature heat capacity can be predicted by applying the classic Neumann-Kopp rule based on the combinations of molar heat capacity of the constituent oxide of MgO and V_2O_5. The thermodynamic properties of MgO and V_2O_5 can be derived from FactSage PS database

Table 3
Enthalpy changes of $Mg_2V_2O_7$ obtained by drop calorimetry.

T/K	$\Delta T\ 298.15H_m/(kJ\cdot mol^{-1})$	T/K	$\Delta T\ 298.15H_m/(kJ\cdot mol^{-1})$	T/K	$\Delta T\ 298.15H_m/(kJ\cdot mol^{-1})$
573	65.66	823	132.81	1073	203.33
623	78.74	873	146.68	1123	217.75
673	92.01	923	160.68	1173	232.28
723	105.46	973	174.79	1223	246.90
773	119.06	1023	189.01	1273	261.61

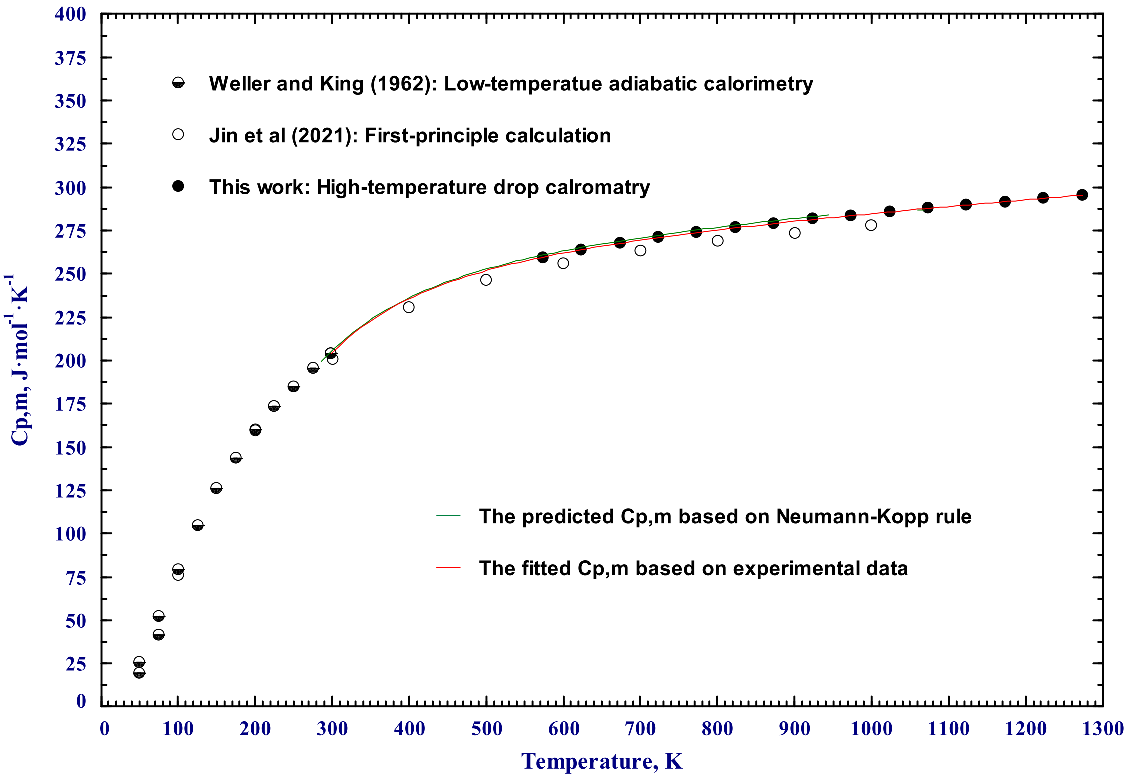

Fig. 10. Molar heat capacity of $Mg_2V_2O_7$ for temperature in the 298.15-1273 K range.

[53]. Good agreement was reached between the estimated values and the present experiment, while, the Neumann-Kopp rule can only be used below the melting point of V_2O_5 (∼943 K). Jin et al. [46] calculated the molar heat capacity of $Mg_2V_2O_7$ based on First-principle calculations, and the results are also shown in Fig. 10. The calculated values are slightly lower than that of the experimental ones. As a result, the predicted *Cp,m* values of $Mg_2V_2O_7$ using the Neumann-Kopp rule and First-principle calculations are not sufficient enough to some extent, especially in high-temperature regions. The reliable experimental data based on calorimetric technology employed in the present work can be applied to thermodynamic database development for V_2O_5-containing systems.

Other thermodynamic functions of the $Mg_2V_2O_7$ related to the reference temperature at 298.15 K can be calculated as follows:

$$\Delta_{298.15}^{T}H_m = \int_{298.15}^{T} CpdT\ (298.15 - 1273K)\ \left(J\cdot mol^{-1}\right) \quad (3)$$

$$\Delta_{298.15}^{T}S_m = \int_{298.15}^{T} Cp/TdT\ (298.15 - 1273K)\ \left(J\cdot mol^{-1}\cdot K^{-1}\right) \quad (4)$$

$$\Delta_{298.15}^{T}G_m = \Delta_{298.15}^{T}H_m - T\Delta_{298.15}^{T}S_m\ (298.15 - 1273K)\left(J\cdot mol^{-1}\right) \quad (5)$$

Based on the measured molar heat capacity at higher temperatures and enthalpy of formation and entropy at 298.15 K from the previous studies [18], the thermodynamic functions of $Mg_2V_2O_7$ can be calculated utilizing Eqs. (3), (4), and (5) for the temperature ranging from 300 to 1273 K. As a result, the reliable thermodynamic data measured by the calorimetric technique can be used with good confidence and expertise to provide further guidelines for selecting precursors to prepare $Mg_2V_2O_7$ via solid-state calcination.

5. Application of thermodynamic properties to materials preparation

The measured thermodynamic properties of $Mg_2V_2O_7$ can be further applied to select the appropriate precursors in the solid-state calcination. In the previous works, MgO, $MgCO_3$, $Mg(OH)_2$, and V_2O_5 were commonly utilized as the precursors to generate $Mg_2V_2O_7$. Chemical reactions of $Mg_2V_2O_7$ formation using different reactive precursors are presented as Eq. (6)-(8):

$$2MgO+V_2O_5=Mg_2V_2O_7 \tag{6}$$

$$2MgCO_3+V_2O_5=Mg_2V_2O_7+2CO_2 \tag{7}$$

$$2Mg(OH)_2+V_2O_5=Mg_2V_2O_7+2H_2O \tag{8}$$

Practically, the most influential factor is the choice of calcination temperature. Gibbs free energy change (ΔG^o) with 1 mol of $Mg_2V_2O_7$ product of chemical reactions (6)-(8) can be calculated using the measured thermodynamic database, and the results are present in Fig. 11. The Gibbs energy of reactions (6), (7), and (8) is negative for temperatures ranging from 300 to 1200 K, confirming that those reactions are always thermodynamically feasible at elevated temperatures. However, the reaction (7) and (8) show much more negative Gibbs free energy than that reaction (6), which means reaction superiority. Compared with 3 different reactions, the chemical reaction of V_2O_5 and $Mg(OH)_2$ for preparing $Mg_2V_2O_7$ is the favorite from a thermodynamic aspect because of thermodynamic superiority.

The V_2O_5 and $Mg(OH)_2$ precursors for preparing $Mg_2V_2O_7$ samples and improving its microwave dielectric properties via solid-state reaction are strongly recommended from a thermodynamic viewpoint. The measured database can also be applied to thermodynamically optimize MgO-V_2O_5 binary, ternary, and multicomponent systems, and provide theoretical calculation and thermodynamic simulation for clean, efficient vanadium extraction from vanadium-bearing slag.

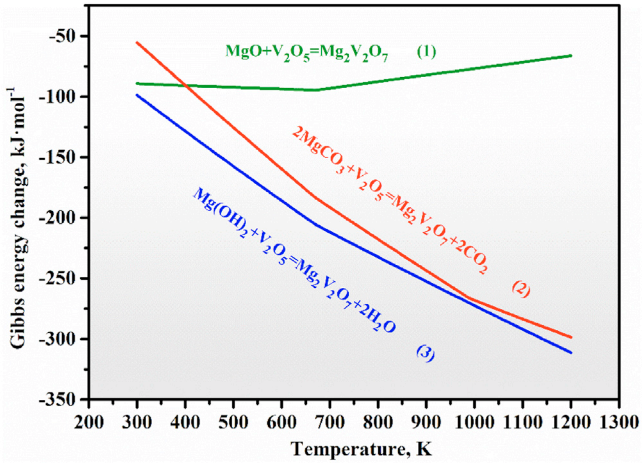

Fig. 11. Gibbs energy change of $Mg_2V_2O_7$ formation.

6. Conclusions

Phase-pure $Mg_2V_2O_7$ was synthesized through solid-state calcination, crystal structure, phase transitions, lattice dynamics, thermal transport, and thermodynamic properties of MgV_2O_7 were systemically studied by experimental techniques and first-principle calculations. The following conclusions were obtained.

1. α-$Mg_2V_2O_7$ crystallizes in monoclinic space group of $P2_1/c$, with cell parameters of a = 6.605(4) Å, b = 8.415(6) Å, c = 9.487(2) Å, and β=100.62(7)°. β-$Mg_2V_2O_7$ crystallizes in triclinic space group $P1$, with the cell parameters of a = 13.759(3) Å, b = 5.435(5) Å, c = 4.930(2) Å, α=81.431(6)°, β=106.892(8)° and γ=130.359(5)°.
2. No imaginary frequency phonon modes are observed, indicating the dynamic stability of the $Mg_2V_2O_7$ compound. Notably, $Mg_2V_2O_7$ has low k_L of 4.77, 5.12, and 4.52 W/mK at room temperature, along the a, b, and c axes, respectively, which originates from the large phonon scatting rate and low phonon group velocity.
3. Enthalpy changes at the phase transitions in $Mg_2V_2O_7$ were measured by performing DSC. The values are equal to 1.82±0.04 kJ/mol, 1.51±0.04 kJ/mol, and 26.54±0.26 kJ/mol for the α-MgV_2O_6↔β-MgV_2O_6 at 743 °C, and β-$Mg_2V_2O_7$↔γ-$Mg_2V_2O_7$ at 908 °C, and incongruent melting at 1083 °C, respectively.
4. The molar heat capacity of $Mg_2V_2O_7$ for the temperature range of 298.15-1273 K was experimentally determined by conducting drop calorimetry, and the dependence was modeled as $Cp=259.19657+0.03105T\text{-}5781130T^2$ ($J\cdot mol^{-1}\cdot K^{-1}$). Other thermodynamic properties can be calculated based on the fitted heat capacity expression at high temperatures.
5. The measured thermodynamic properties were applied to evaluate the reaction behavior of $Mg_2V_2O_7$ generation via a solid-state reaction, indicating that the V_2O_5 and $Mg(OH)_2$ precursors are strongly recommended due to their thermodynamic superiority.

Declaration of competing interest

The authors declare that they have no known competing financial interests or personal relationships that could have appeared to influence the work reported in this paper.

Acknowledgments

This work was supported by the National Key Research and Development Program of China (No. 2022YFC3901001-1), and the National Natural Science Foundation of China (Grant No. U1902217). Guishang Pei acknowledges financial support from the Chinese Scholarship Council (CSC No. 202106050084).

References

[1] R.R. Tummala, J. Am. Ceram. Soc. 74 (5) (1991) 895–908, doi:10.1111/j.1151-2916.1991.tb04320.x.

[2] Y. Guo, H. Ohsato, K. Kakimoto, J. Eur. Ceram. Soc. 26 (10–11) (2006) 1827–1830, doi:10.1016/j.jeurceramsoc.2005.09.008.

[3] M.T. Sebastian, Dielectric Materials For Wireless Communication, Elsevier, 2010.

[4] J. Wang, L. Meng, Z. Zhang, B. Sa, X. Fu, L. Sheng, D. Xu, Y. Zheng, J. Magn. Alloys 11 (3) (2023) 1074–1082, doi:10.1016/j.jma.2021.07.011.

[5] J. Wang, L. Meng, W. Xie, C. Ji, R. Wang, P. Zhang, L. Jin, L. Sheng, Y. Zheng, J. Magn. Alloys (2022), doi:10.1016/j.jma.2022.09.025.

[6] Z. Ding, H. Li, L. Shaw, Chem. Eng. J. 385 (2020) 123856, doi:10.1016/j.cej.2019.123856.

[7] Z. Ding, Z. Chen, T. Ma, C.T. Lu, W. Ma, L. Shaw, Energy Storage Mater. 27 (2020) 466–477, doi:10.1016/j.ensm.2019.12.010.

[8] Y. Chen, X. Guo, Q. Wang, Q. Tian, S. Huang, J. Zhang, Tungsten 3 (3) (2021) 348–360, doi:10.1007/s42864-021-00090-w.

[9] M.R. Joung, J.S. Kim, M.E. Song, S. Nahm, J.H. Paik, J. Am. Cream. Soc. 92 (12) (2009) 3092–3094, doi:10.1111/j.1551-2916.2009.03324.x.

[10] M.R. Joung, J.S. Kim, M.E. Song, J.H. Choi, J.W. Sun, S. Nahm, J.H. Paik, B.H. Choi, J. Am. Cream. Soc. 92 (9) (2009) 2151–2154, doi:10.1111/j.1551-2916.2009.03179.x.

[11] Q. Li, X. Peng, F. Pan, J. Magn. Alloys 9 (6) (2021) 2223–2224, doi:10.1016/j.jma.2021.11.003.

[12] D. Li, Y. Yuan, J. Liu, M. Fichtner, F. Pan, J. Magn. Alloys 8 (4) (2020) 963–979, doi:10.1016/j.jma.2020.09.017.

[13] M.R. Joung, J.S. Kim, M.E. Song, S. Nahm, J.H. Paik, B.H. Choi, J. Am. Cream. Soc. 92 (7) (2009) 1621–1624, doi:10.1111/j.1551-2916.2009.03078.x.

[14] T. Zhang, Q. Gui, Y. Zhou, J. Yang, H. Zeng, Q. Peng, Q. Ye, D. Yang, Y. Li, Comput. Theor. Chem. 1220 (2023) 113988, doi:10.1016/j.comptc.2022.113988.

[15] D.A. Vinnik, I.P. Prosvirin, V.E. Zhivulin, N. Wang, X. Jiang, E.A. Trofimov, O.V. Zaitseva, S.A. Gudkova, S. Nemrava, D.A. Zherebtsov, R. Niewa, V.V. Atuchin, Z. Lin, J. Alloys Compd. 844 (2020) 156036.

[16] N.O. Azarapin, V.V. Atuchin, N.G. Maximov, A.S. Aleksandrovsky, M.S. Molokeev, A.S. Oreshonkov, N.P. Shestakov, A.S. Krylov, T.M. Burkhanova, S. Mukherjee, O.V. Andreev, Mater. Res. Bull. 140 (2021) 111314.

[17] Y. Denisenko, V.V. Atuchin, M.S. Molokeev, A.E. Sedykh, N.A. Khritokhin, A.S. Aleksandrovsky, A.S. Oreshonkov, N.P. Shestakov, S.V. Adichtchev, A.M. Pugachev, Molecules 27 (13) (2022) 3966, doi:10.3390/molecules27133966.

[18] M.Y. Khodos, V. Zhuravlev, A. Fotiev, Inorg. Mater. 15 (1) (1979) 98–99.

[19] J. Leitner, P. Voňka, D. Sedmidubský, P. Svoboda, Thermochim. Acta 497 (1) (2010) 7–13, doi:10.1016/j.tca.2009.08.002.

[20] H. Kopp, Proc. R. Soc. Lond. 13 (1992) 229–239.

[21] J. Leitner, P. Chuchvalec, D. Sedmidubský, A. Strejc, P. Abrman, Thermochim. Acta 395 (1) (2002) 27–46, doi:10.1016/S0040-6031(02)00177-6.

[22] Z. Cao, N. Wang, W. Xie, Z. Qiao, I.H. Jung, Calphad 56 (2017) 72–79.

[23] G. Kresse, J. Hafner, Phys. Rev. B 48 (17) (1993) 13115, doi:10.1103/PhysRevB.48.13115.

[24] G. Kresse, J. Furthmüller, Phys. Rev. B 54 (16) (1996) 11169, doi:10.1103/PhysRevB.54.11169.

[25] P.E. Blöchl, Phys. Rev. B 50 (24) (1994) 17953, doi:10.1103/PhysRevB.50.17953.

[26] J.P. Perdew, A. Ruzsinszky, G.I. Csonka, O.A. Vydrov, G.E. Scuseria, L.A. Constantin, X. Zhou, K.J. Burke, Phys. Rev. Lett. 100 (13) (2008) 136406, doi:10.1103/PhysRevLett.100.136406.

[27] H.J. Monkhorst, J.D. Pack, Phys. Rev. B 13 (12) (1976) 5188, doi:10.1103/PhysRevB.13.5188.

[28] A. Togo, I. Tanaka, Script Mater. 108 (2015) 1–5, doi:10.1016/j.scriptamat.2015.07.021.

[29] W. Li, J. Carrete, N.A. Katcho, N.J. Mingo, Comput. Phys. Commun. 185 (6) (2014) 1747–1758, doi:10.1016/j.cpc.2014.02.015.

[30] P. Jiang, X. Yu, Y. Xiao, S. Zhao, W. Peng, Tungsten (2022) 1–12, doi:10.1007/s42864-022-00195-w.

[31] I. Barin, Thermochemical Data of Pure Substances, 3rd ed., VCH, 2008.

[32] D.A. Ditmars, S. Ishihara, S.S. Chang, G. Bernstein, E.D. West, J. Res. Nat. Bur. Stand. 87 (2) (1982) 159.

[33] G. Pei, J. Xiang, L. Yang, X. Jin, X. Lv, Calphad 70 (2020) 101802, doi:10.1016/j.calphad.2020.101802.

[34] G. Pei, J. Xiang, G. Li, S. Wu, F. Pan, X. Lv, in: 10th International Symposium on High-Temperature Metallurgical Processing, Springer, 2019, pp. 569–577, doi:10.1007/978-3-030-05955-2_54.

[35] G. Pei, J. Xiang, X. Lv, G. Li, S. Wu, D. Zhong, W. Lv, J. Alloys Compd. 794 (2019) 465–472, doi:10.1016/j.jallcom.2019.04.186.

[36] G. Pei, J. Xiang, Q. Huang, X.J. Lv, J. Am. Cream. Soc. (2022), doi:10.1111/jace.18592.

[37] G. Pei, J. Xiang, I.-H. Jung, M. Jiao, Z. Li, X. Lv, J. Am. Cream. Soc. 106 (4) (2023) 2529–2538, doi:10.1111/jace.18944.

[38] D. Ditmars, S. Ishihara, S. Chang, G. Bernstein, E. West, J. Res. Natl. Bur. Stand. 87 (2) (1982) 159–163.

[39] P.G. Gagarin, A.V. Tyurin, V.N. Guskov, A.V. Khoroshilov, G.E. Nikiforova, K.S. Gavrichev, Inorg. Mater. (2017), doi:10.1134/S0020168517060048.

[40] V.N. Guskov, A.V. Khoroshilov, M.A. Ryumin, O.N. Kondrat'Eva, K.S. Gavrichev, Ceram. Int. 46 (4) (2019), doi:10.1016/j.ceramint.2019.10.296.

[41] G. Pei, C. Pan, D. Zhong, J. Xiang, X. Lv, J. Magn. Alloys (2022), doi:10.1016/j.jma.2022.05.011.

[42] E.V. Alekseev, O. Felbinger, S. Wu, T. Malcherek, W. Depmeier, G. Modolo, T.M. Gesing, S.V. Krivovichev, E.V. Suleimanov, T.A. Gavrilova, L.D. Pokrovsky, A.M. Pugachev, N.V. Surovtsev, V.V. Atuchin, J. Solid State Chem. 204 (2013) 59–63, doi:10.1016/j.jssc.2013.04.038.

[43] V.V. Atuchin, A.S. Aleksandrovsky, M.S. Molokeev, A.S. Krylov, A.S. Oreshonkov, D. Zhou, J. Alloys Compd. 729 (2017) 843–849, doi:10.1016/j.jallcom.2017.07.259.

[44] Y.N. Zhuravlev, V.V. Atuchin, Nanomaterials 10 (11) (2020) 2275, doi:10.3390/nano10112275.

[45] V. Grossman, V. Atuchin, B.G. Bazarov, A. Aleksandrovsky, E. Eremin, A. Krylov, N. Kuratieva, J.G. Bazarova, N. Maximov, M.J. Molokeev, Molecules 28 (4) (2023) 1629, doi:10.3390/molecules28041629.

[46] X. Jin, R. Wang, Y. Zhou, J. Lai, J. Li, G. Pei, S. Chen, X. Wang, J. Xiang, Z. Zhu, X. Lv, J. Alloys Compd. 896 (2022), doi:10.1016/j.jallcom.2021.162862.

[47] R. Wollast, A.J. Tazairt, Silicates Ind. 34 (1969) 37–45.

[48] G. Clark, R. Morley, J. Solid State Chem. 16 (3–4) (1976) 429–435, doi:10.1016/0022-4596(76)90060-8.

[49] Z. Cao, N. Wang, W. Xie, Z. Qiao, I.H. Jung, Calphad 56 (2017) 72–79, doi:10.1016/j.calphad.2016.12.001.

[50] A.J. Pollard, Proposed Phase Diagram for the System Magesium Oxide-Vanadium Pentoxide, 1964 Issue NASA Accession No. N65-17008, Contract No. NPL-6O38.

[51] E.J. Speranskaya, Neorg. Mater. 7 (1971) 1804–1807.

[52] C.G. Maier, K.K. Kelley, J. Am. Ceram. Soc. 54 (8) (1932) 3243–3246, doi:10.1021/ja01347a029.

[53] C.W. Bale, P. Chartrand, S.A. Degterov, G. Eriksson, K. Hack, R.B. Mahfoud, J. Melançon, A.D. Pelton, S. Petersen, Calphad 33 (2) (2002) 295–311, doi:10.1016/S0364-5916(02)00035-4.